



# Nitrogen vacancy engineered graphitic C<sub>3</sub>N<sub>4</sub>-based polymers for photocatalytic oxidation of aromatic alcohols to aldehydes

Jing Ding<sup>a</sup>, Wei Xu<sup>a</sup>, Hui Wan<sup>a</sup>, Dashui Yuan<sup>a</sup>, Chong Chen<sup>a</sup>, Lei Wang<sup>a</sup>, Guofeng Guan<sup>a,\*</sup>, Wei-Lin Dai<sup>b,\*</sup>

<sup>a</sup> State Key Laboratory of Materials-Oriented Chemical Engineering, College of Chemical Engineering, Jiangsu National Synergetic Innovation Center for Advanced Materials, Nanjing Tech University, Nanjing 210009, PR China

<sup>b</sup> Department of Chemistry & Shanghai Key Laboratory of Molecular Catalysis and Innovative Materials, Fudan University, Shanghai 200433, PR China

## ARTICLE INFO

### Keywords:

Graphitic carbon nitride  
Nitrogen vacancy  
Photocatalysis  
Aromatic alcohols  
Organic dyes

## ABSTRACT

Vacancy defect in the semiconductors plays an important role in the improvement of the electronic structure and the increase of specific reaction sites for reactant molecules, and consequently enhancing the photocatalytic activity of semiconductor photocatalysts. Through high-temperature thermal condensation of a nitric acid-pretreated melamine precursor, nitrogen vacancies were successfully introduced in the framework of g-C<sub>3</sub>N<sub>4</sub>. The nitrogen vacancies located at the uncondensed terminal NH<sub>x</sub> lattice sites were conducive to the enhancement of optical absorption, the improvement of the separation efficiency of the photogenerated charge carrier and the increase of surface area, which was beneficial to the photocatalytic oxidation process. More significantly, the novel CNNA(X) were used as efficient photocatalysts in the green process of aromatic aldehydes from the photocatalytic selective oxidation of aromatic alcohols and the photocatalytic degradation of organic pollutants. CNNA(X) samples exhibited enhanced photocatalytic activity and excellent recyclability and stability. The 68.3% benzyl alcohol conversion and almost 100% selectivity was observed for the CNNA (0.9) photocatalyst, higher than that of pure g-C<sub>3</sub>N<sub>4</sub>. Meanwhile, CNNA (0.9) showed superior photocatalytic degradation performance of organic dyes (RhB and MO). Furthermore, the underlying photocatalytic oxidation mechanism was proposed by the controlled experiments using radical scavengers.

## 1. Introduction

Selective oxidation of aromatic alcohols to their corresponding aldehydes or ketones plays a key role in organic synthesis and chemical industry. For instance, benzaldehyde, one of the most important value-added products for the industrial synthesis of bulk and fine chemicals, has been applied in perfumery, dyestuff, pharmaceutical industries, etc [1–3]. However, commercial production of benzaldehyde using traditional synthesis method has obvious drawbacks, including toxic or expensive oxidant (Br<sub>2</sub>, CrO<sub>3</sub>, KMnO<sub>4</sub>, etc.), harsh reaction conditions (high temperature and high pressure) and expensive catalysts (precious metal catalysts such as Pd, Pt, etc) [4–7]. Accordingly, the exploration of a highly effective and environmental-benign catalytic route for the industrial production of benzaldehyde under moderate conditions is necessary.

The exploitation of sunlight, by virtue of the sun's great potential as a source of clean, renewable and economical energy, has been a general concern in the world. Solar energy-driven semiconductor photocatalysis

has emerged as one of the most promising and environmental-friendly technologies in the field of contamination elimination, energy conversion and fine chemicals production [8–12]. Titanium dioxide (TiO<sub>2</sub>), owing to its outstanding stable physicochemical properties (such as its superior chemical stability, strong oxidation ability, nontoxicity, etc.), has been extensively used as one of the most ideal candidates in the field of semiconductor photocatalysis for the water splitting, degradation of organic pollutants and selective organic transformation [13–18]. However, photocatalytic selective oxidation of alcohols to the corresponding aldehydes using TiO<sub>2</sub> photocatalyst still remains a great challenge. The high oxidation potential (2.7 eV) makes hydroxyl radicals (·OH) easy to generate and always causes over-oxidation of alcohols to produce by-products (such as acids or CO<sub>2</sub>), thus leading to low selectivity of aldehyde. Synchronously, TiO<sub>2</sub> merely absorbs ultraviolet irradiation, which accounts for about 4% of sunlight, greatly limiting its practical applications. Therefore, a great vision has come toward the development of an efficient and stable photocatalyst that can make full use of solar energy and participate in the selective organic

\* Corresponding authors.

E-mail addresses: [guangf@njtech.edu.cn](mailto:guangf@njtech.edu.cn) (G. Guan), [wldai@fudan.edu.cn](mailto:wldai@fudan.edu.cn) (W.-L. Dai).

<http://dx.doi.org/10.1016/j.apcatb.2017.09.048>

Received 11 August 2017; Received in revised form 13 September 2017; Accepted 21 September 2017

Available online 22 September 2017

0926-3373/ © 2017 Published by Elsevier B.V.

transformation under simulated sunlight irradiation.

Polymeric graphitic carbon nitride ( $g\text{-C}_3\text{N}_4$ ), made of earth-abundant elements, has recently received a great deal of interest in a variety of applications [19–23]. Its diverse physicochemical properties such as excellent thermal and chemical stability, nontoxic, narrow optical band structure (band gap is 2.70 eV with theoretical calculated CB and VB edge potentials are  $-1.13$  and  $1.57$  eV, respectively) and tunable electronic structure make it to be a kind of promising photocatalyst in solar to chemical energy conversion processes (such as photocatalytic  $\text{H}_2$  production,  $\text{CO}_2$  reduction and selective organic transformation). Unfortunately, the photocatalytic performance of pristine  $g\text{-C}_3\text{N}_4$  is restricted by inherent low quantum efficiency, small BET surface area and high recombination rate of electron-hole pairs. Tremendous efforts have been made to manipulate  $g\text{-C}_3\text{N}_4$ , including loading metal or non-metal, constructing heterojunctions with other semiconductors and chemical doping with foreign elements. Nevertheless, there is still plenty of space to explore a new fundamental approach besides currently employed strategies.

Vacancy defects in the semiconductors play an important role in the improvement of the electronic structure and the increase of specific reaction sites for reactant molecules, and consequently enhancing the photocatalytic activity of semiconductor photocatalysts. The structure defects can act as trapping sites for photoinduced carriers and restrain the recombination of photogenerated electrons and holes, thus improving the overall quantum efficiency [24,25]. Simultaneously, mid-gap states, commonly regarded as band tail states overlapping with conduction band or valence band, can be subsequently generated when vacancy defects of the semiconductors appear, which can serve as active center of photogenerate electron-hole excitation and prolong the optical response [26,27]. Recently, studies on the vacancy defects that help improve the photocatalytic activity of  $g\text{-C}_3\text{N}_4$  photocatalyst have been intensively explored. Chen et al. reported that the defective  $g\text{-C}_3\text{N}_4$  was prepared by different atmospheres treatment and found that  $g\text{-C}_3\text{N}_4$  treated by hydrogen gas produced the highest amount of  $\text{H}_2$  (approximately  $5.0 \mu\text{mol/g}$ ) under 5 h of visible light irradiation, which can be attributed to the formation of two-coordinated nitrogen vacancy in  $g\text{-C}_3\text{N}_4$  and thus narrowing band gap and enhancing solar absorption [28]. Gao et al. demonstrated that nitrogen-deficient graphitic carbon nitride, prepared by hydrothermal treatment with ammonium thiosulfate as an oxidant, exhibited greatly enhanced photocatalytic activity, which could be ascribed to the deficiency of the terminal amino species on the framework of  $g\text{-C}_3\text{N}_4$  [29]. Inspired by these findings, it is expected that introducing nitrogen vacancies in carbon nitride can be an effective strategy to optimize the photocatalytic activity of carbon nitride. However, little information is still available on the correlation between the nitrogen vacancies in the framework of  $g\text{-C}_3\text{N}_4$  and the photocatalytic oxidation activity, especially only few studies have intensively explored the effects of nitrogen vacancies on the electronic structure and chemical properties of  $g\text{-C}_3\text{N}_4$ , so as to affect the photocatalytic oxidation performance of aromatic alcohols.

Herein, we report defective  $g\text{-C}_3\text{N}_4$  nanosheets were fabricated by introducing nitrogen vacancies in the framework of  $g\text{-C}_3\text{N}_4$  with high-temperature thermal condensation of nitric acid-pretreated melamine

as a precursor. Detailed investigations on the effects of nitrogen vacancies on the electronic structure and chemical properties of  $g\text{-C}_3\text{N}_4$  were carried out. Moreover, the defective  $g\text{-C}_3\text{N}_4$  nanosheets were used as photocatalysts for the aerobic oxidation of aromatic alcohols with molecular oxygen as oxidant under simulated sunlight irradiation and the photocatalytic degradation of organic pollutants. Furthermore, the stability of the defective  $g\text{-C}_3\text{N}_4$  photocatalyst was further studied and the possible photooxidation mechanism was proposed in detail.

## 2. Experimental

### 2.1. Materials

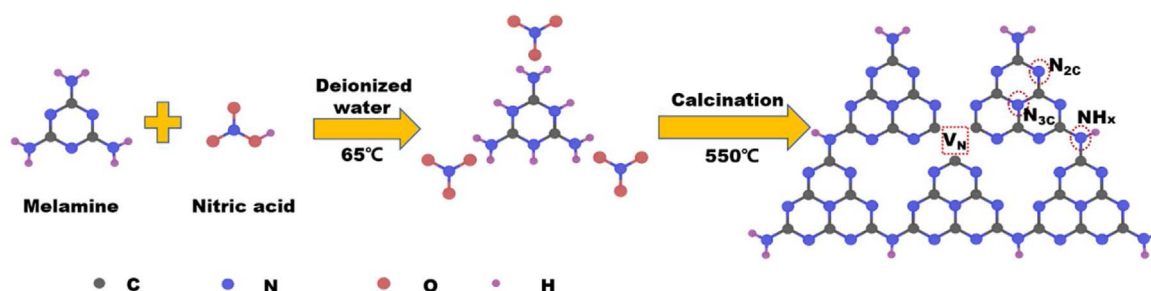
Melamine (99.0%, AR), nitric acid (65.0%, AR) and *p*-nitro benzyl alcohol (98.0%, AR) were purchased from Aladdin Industrial Inc. Benzyl alcohol (99.0%, AR), benzaldehyde (98.5%, AR), *p*-methyl benzyl alcohol (99.0%, AR), toluene (99.5%, AR), acetonitrile (99.0%, AR), dimethyl carbonate (99.0%, AR) and tributyl phosphate (98.5%, AR) were purchased from Sinopharm Chemical Reagent Co. Ltd. All of the reagents were analytical grade and used without any further purification.

### 2.2. Catalyst preparation

Melamine powder (7.57 g, 0.06 mol) was dispersed in 50 mL deionized water and heated at  $65^\circ\text{C}$  for 1 h under stirring. Then, a certain amount of nitric acid (65.0 wt.%) were added to the above solution and kept at  $65^\circ\text{C}$  until white solid precipitation was obtained and the temperature was risen to  $100^\circ\text{C}$  for complete water evaporation, followed by milling and annealing at  $550^\circ\text{C}$  under air atmosphere for 3 h with ramping rate of  $5^\circ\text{C}/\text{min}$ . After cooling to room temperature, the products were obtained. The as-prepared defective  $g\text{-C}_3\text{N}_4$  catalysts were denoted as CNNA (X) in which X stood for the mole ratio of nitric acid to melamine. Meanwhile, pure  $g\text{-C}_3\text{N}_4$  nanosheets (CN) were prepared under identical conditions as the synthesis of CNNA (X) but without nitric acid addition. The detailed schematic illustration of the synthesis of CNNA (X) could be identified during the preparation process, as described in Scheme 1.

### 2.3. Characterizations

The X-ray diffraction (XRD) patterns were recorded on a Bruker D8 advance spectrometer with  $\text{Cu K}\alpha$  radiation ( $\lambda = 0.154 \text{ nm}$ ), operated at 40 mA and 40 kV. The FT-IR spectra were carried out on a Nicolet Avatar-360 FT-IR spectrometer. The X-ray photoelectron spectra (XPS) were obtained on a RBD 147 upgraded PHI 5000C ESCA system equipped with a dual X-ray source, of which the  $\text{Mg K}\alpha$  (1253.6 eV) anode and a hemispherical energy analyzer were used. The background pressure during data acquisition was maintained at  $< 10^{-6} \text{ Pa}$ . Measurements were performed at a pass energy of 93.90 eV. All binding energies were calibrated using contaminant carbon ( $\text{C1s} = 284.6 \text{ eV}$ ). Transmission electron microscope (TEM) images were obtained on a JOEL JEM 2010 transmission electron microscope. The samples were



Scheme 1. The detailed illustration of the synthesis of CNNA (X) system.

supported on carbon-coated copper grids for the experiment. The Laser Raman experiments were performed with a Jobin Yvon Dilor Labram I Raman spectrometer equipped with a holographic notch filter, CCD detector, and He-Ne laser radiating at 632.8 nm. UV–vis diffuse reflectance spectroscopy measurement was carried out on a Shimadzu UV-3600 UV-vis-NIR spectrophotometer with BaSO<sub>4</sub> as a reflectance standard. The specific surface areas ( $S_{\text{BET}}$ ) were obtained from N<sub>2</sub> adsorption-desorption isotherms at 77 K (ASAP 2010, Micromeritics USA) on the samples preheated at 120 °C for 12 h in vacuum. The  $S_{\text{BET}}$  values were calculated using the Brunauer, Emmett and Teller (BET) method. CHN elemental analysis was performed on a Vario EL Cube elemental analyzer. Time-resolved PL fluorescence spectra of the solution were obtained using a FLS920 spectrometer (Edinburgh Instruments). The excitation wavelength is 360 nm and the probe wavelength is 460 nm. Photoluminescence spectra (PL) of the samples were obtained using a fluorescence spectrometer (Hitachi F-4500) using a Xe lamp as excitation source. Electrochemical impedance spectroscopy (EIS), performed on CHI 660C electrochemical workstation (Shanghai Chenhua Instruments Co.), were interpreted by a nonlinear least-squares fitting procedure using the Zsimpwin software at an AC voltage magnitude of 5 mV in the frequency of 10<sup>-1</sup> Hz–10<sup>6</sup> Hz. The photocurrent performances were assessed via an I–T curve (a function of current to time) on the CHI 660C electrochemical workstation (Shanghai Chenhua Instruments Co.). Four cycles were applied and the intermission for turn on/off light was 30 s.

#### 2.4. Evaluation of photocatalytic performance

The photooxidation of aromatic alcohols was performed in a 100 mL of homemade quartz reactor with O<sub>2</sub> atmosphere under simulated sunlight irradiation at different temperature. The specific reactor is shown in Fig. S1. For each measurement, the photocatalyst (20 mg) was suspended in 10 mL of solvent. Subsequently, aromatic alcohol (1 mmol) as reactant and methylbenzene (0.37 mmol) as internal standard were added into the above solution. Prior to irradiation, the reactor was saturated with O<sub>2</sub> and magnetically stirred in the darkness for 30 min to reach the absorption-desorption equilibrium. The reaction was performed under the irradiation of a 300 W Xe lamp without UV and IR cut-off filters. During the photooxidation reaction, 10 µL of suspension with catalyst was sampled at constant intervals and centrifuged to remove the solid particles. The obtained products were determined by a gas chromatograph (GC7900, Techcomp. Ltd., China) with an InertCap WAX capillary column and a FID detector. The values of the conversion of aromatic alcohols, selectivity and yield of aromatic aldehydes were calculated based on three parallel experiments. In the photooxidation stability experiments, the catalysts were centrifuged, washed several times with alcohol and water, dried and then re-dispersed in solution with aromatic alcohols for next cycle.

### 3. Results and discussion

#### 3.1. Catalyst characterization

The structure properties and compositions of the as-prepared samples were investigated by X-ray diffractions (XRD). As shown in Fig. 1a, g-C<sub>3</sub>N<sub>4</sub> and CNNA (X) catalysts exhibited a similar layered structure with two pronounced diffraction peaks at 2θ values of approximately 13.3° and 27.5°, which matched well with the (100) and (002) diffraction peaks of layered g-C<sub>3</sub>N<sub>4</sub>. The former peak at 13.3° could be ascribed to in-planar tris-s-triazine structural packing with the distance around 0.665 nm. The latter one at 27.5° with a much stronger intensity was a characteristic interlayer stacking reflection of the conjugated aromatic systems with interlayer distance around 0.324 nm [30,31]. Compared with pure g-C<sub>3</sub>N<sub>4</sub>, the (002) diffraction peak position for CNNA (X) in Fig. 1b gradually shifted to the higher angle, indicating that some kind of lattice of g-C<sub>3</sub>N<sub>4</sub> framework changed and a slight

decrease in the interlayer stacking distance and an increase of interlayer stacking density happened, well aligned with the literatures reported previously [32]. Simultaneously, the (100) diffraction peak of CNNA (X) at around 13.1° also grew weaker than that of pure g-C<sub>3</sub>N<sub>4</sub>, especially CNNA (0.9), further implying that much lowered long-range order of the in-plane structural packing of CNNA sample existed. Therefore, the direct condensation of the nitric acid pretreated melamine certainly resulted in the partial loss of lattice nitrogen so that the distance between the interlayer stacking of g-C<sub>3</sub>N<sub>4</sub> decreased.

The chemical structure of g-C<sub>3</sub>N<sub>4</sub> and CNNA (X) samples were further analyzed by FTIR spectra, as presented in Fig. 2. Both g-C<sub>3</sub>N<sub>4</sub> and CNNA (X) samples exhibited the typical IR patterns of graphitic carbon nitride, illustrating that the basic atomic structure of g-C<sub>3</sub>N<sub>4</sub> still remained after the precursor melamine pre-treated with nitric acid. A broad peak at around 3000–3500 cm<sup>-1</sup> revealed the existence of the primary and secondary amines and O–H stretching vibrations of surface-absorption water molecules. Since the primary and secondary amines stretching vibrations were completely shrouded by hydroxyl species in the same location region, it was difficult to judge the variation of the primary and secondary amines. Meanwhile, the sharp absorption band centered at around 810 cm<sup>-1</sup> originated from the out-of-plane bending mode of heptazine rings, indicating the existence of the basic melon units with –NH/–NH<sub>2</sub> groups [33]. Additionally, the absorption bands in the region ranging from 900 to 1800 cm<sup>-1</sup> were assigned to C–N–C and C=N stretching vibration modes of heterocycles, associated with skeletal stretching vibrations of aromatic rings [34]. Obviously, the peak at around 810 cm<sup>-1</sup> shifted toward low frequency and the intensities of the absorption peaks below 2000 cm<sup>-1</sup> decreased after the precursor melamine pretreated with nitric acid, suggesting the existence of nitrogen vacancies in the framework of g-C<sub>3</sub>N<sub>4</sub>.

To better understand the effects of nitrogen vacancies on the electronic band structure and optical properties of g-C<sub>3</sub>N<sub>4</sub>, UV–vis diffuse reflectance spectra (UV–vis DRS) was carried out. As demonstrated in Fig. 3a, pure g-C<sub>3</sub>N<sub>4</sub> showed a typical semiconductor absorption in a wide range of UV to visible light wavelength, whose absorption edge was located approximately at 460 nm. Interestingly, with the introduction of nitrogen vacancies in g-C<sub>3</sub>N<sub>4</sub> skeleton, the absorption edges of CNNA (X) samples exhibited a significant red-shift absorption. The CNNA (X) samples displayed improved light absorption in UV and visible-light regions. Undoubtedly, the introduction of nitrogen vacancies remarkably altered its own electronic structure and light-harvesting ability, conducive to the production of more photogenerated electrons and holes needed for the photocatalytic reactions, further resulting in enhanced photocatalytic properties. In addition, the band gaps energies (Fig. 3b) calculated based on the Oregan and Gratzel method of g-C<sub>3</sub>N<sub>4</sub>, CNNA (0.3), CNNA (0.9), CNNA (1.5) and CNNA (2.1) samples were 2.70 eV, 2.62 eV, 2.45 eV, 2.25 eV and 2.06 eV, respectively. Obviously, the nitrogen vacancies existing in the bulk g-C<sub>3</sub>N<sub>4</sub> presumably created a partial overlap of defect-related states and the band gap energies slightly narrowed accompanied with the increasing ratio of nitric acid and melamine as precursors, implying that the introduction of nitrogen vacancies in the g-C<sub>3</sub>N<sub>4</sub> matrix strongly affected the optical property and electronic band structure of g-C<sub>3</sub>N<sub>4</sub> photocatalyst.

The Raman spectra, as shown in Fig. 4, illustrated additional information for the structures of g-C<sub>3</sub>N<sub>4</sub> and CNNA (X) samples. The characteristic peaks of g-C<sub>3</sub>N<sub>4</sub> at 712, 988, 1217 and 1570 cm<sup>-1</sup> were observed (see Fig. 4a). The observed Raman bands at approximately 712 and 988 cm<sup>-1</sup> were indexed to the different types of ring breathing modes of s-triazine in the g-C<sub>3</sub>N<sub>4</sub> crystal structure. The peak at around 1570 cm<sup>-1</sup> could be assigned to the stretching vibration of s-triazine ring. Notably, when the nitrogen vacancies were introduced into the skeleton of g-C<sub>3</sub>N<sub>4</sub>, there was no obvious change in the Raman pattern of CNNA samples compared with g-C<sub>3</sub>N<sub>4</sub>. However, the absorption peaks at 712 and 988 cm<sup>-1</sup> for CNNA samples became broader and weaker and a distinct shift to higher wavenumber appeared, as shown

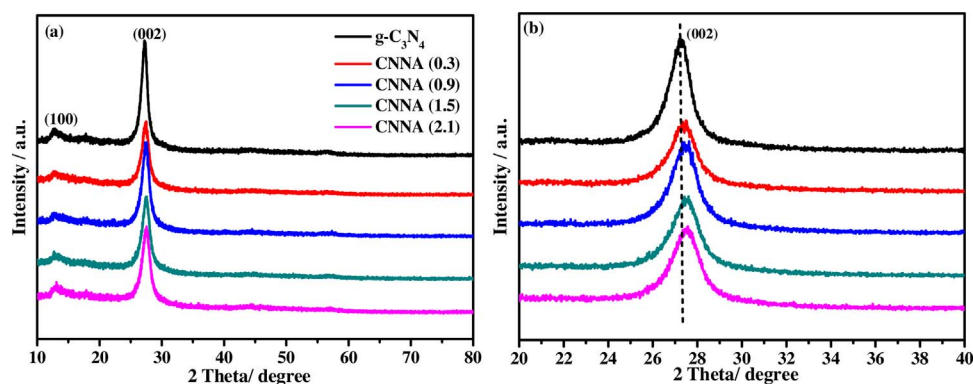


Fig. 1. XRD patterns of g-C<sub>3</sub>N<sub>4</sub> and CNNA (X) systems (a) and magnification of the corresponding (002) peak of g-C<sub>3</sub>N<sub>4</sub> and CNNA (X).

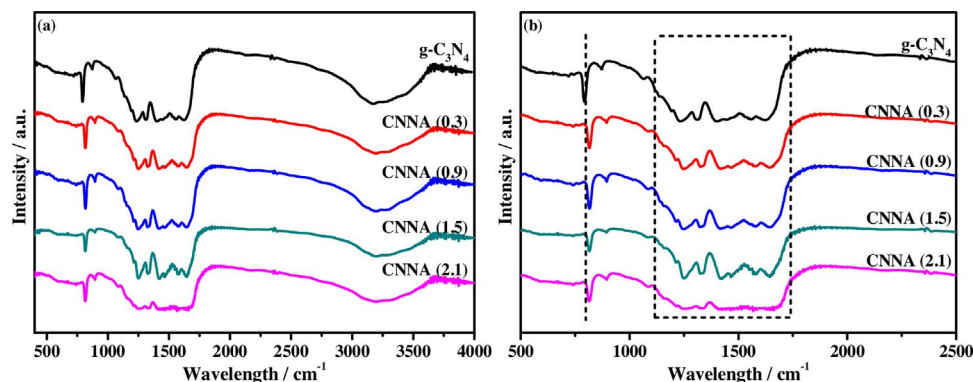


Fig. 2. FT-IR spectra (a) and partial magnification of the characteristic peaks (b) of g-C<sub>3</sub>N<sub>4</sub> and CNNA (X) samples.

in Fig. 4b. This phenomenon may be attributed to the crystalline defects within the framework of g-C<sub>3</sub>N<sub>4</sub> could strongly affect the characteristic vibrational frequency of pure g-C<sub>3</sub>N<sub>4</sub>, well consistent with the results of XRD and FTIR.

The nitrogen adsorption and desorption isotherms were applied to characterize the specific surface area of g-C<sub>3</sub>N<sub>4</sub> and CNNA system, as listed in Table S1. The BET surface areas ( $S_{\text{BET}}$ ) of CNNA (X) initially increased from 12 to 23 m<sup>2</sup> g<sup>-1</sup>, then a slightly decrease to 17 m<sup>2</sup> g<sup>-1</sup> appeared. Interestingly, the BET surface area obviously increased after nitrogen vacancies introduced, even the  $S_{\text{BET}}$  of CNNA (0.9) increased by nearly 2 times as that of the pristine g-C<sub>3</sub>N<sub>4</sub>, suggesting that g-C<sub>3</sub>N<sub>4</sub> nanosheets were unfolded by the introduction of nitrogen vacancies to increase the BET surface area. The larger  $S_{\text{BET}}$  would contribute to facilitating adsorption, desorption and diffusion of reactants and products and meanwhile providing more reaction sites, which was conducive to the enhanced photooxidation performance. The transmission electron microscopy (TEM) image of pure g-C<sub>3</sub>N<sub>4</sub> in Fig. S2a displayed a graphite-like lamellar structure with wrinkling and rolling edges structure. With the introduction of nitrogen vacancies in g-C<sub>3</sub>N<sub>4</sub> skeleton, the

morphology of CNNA (0.9) sample kept almost no change, besides a spot of irregular porous structure (Fig. S2b and S2d). This porous structure could be attributed to the removal of NH<sub>x</sub> species during the high-temperature thermal condensation, which was proved by the results of the nitrogen adsorption and desorption isotherms in Table S1. In addition, the energy dispersive X-ray spectroscopy (EDX) shown in Fig. S2c, resulting from selected area, revealed that C and N elements existed in the CNNA system.

To investigate in-depth the surface chemical states and electronic structure changes of CNNA systems, X-ray photoelectron spectroscopy (XPS) was carried out. Fig. 5a displayed that two obvious peaks with binding energies of 284.6 eV and 287.5 eV could be respectively ascribed to the adventitious carbon and three-coordinated C atoms (C<sub>3c</sub>) in g-C<sub>3</sub>N<sub>4</sub> sample [35]. Obviously, the C1s binding energy of C<sub>3c</sub> shifted from 287.5 eV for g-C<sub>3</sub>N<sub>4</sub> to 287.8 eV for CNNA (0.9). This phenomenon could be ascribed to the extra electrons redistribution of CNNA system compared to pristine g-C<sub>3</sub>N<sub>4</sub>. As shown in Fig. 5b, for pure g-C<sub>3</sub>N<sub>4</sub>, the N1s spectra could be deconvoluted into three peaks with binding energy at 397.9, 398.7 and 400.4 eV, respectively [36]. The

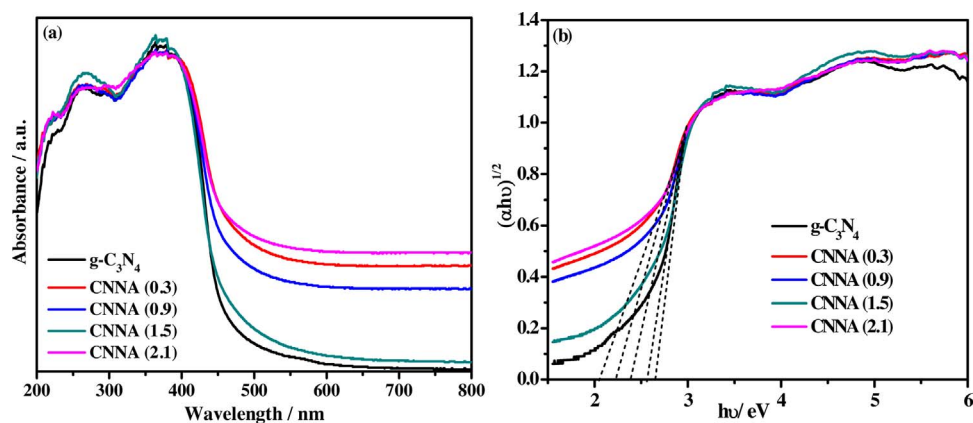


Fig. 3. UV-vis absorption spectra (a) and band gap energies (b) of CNNA system.



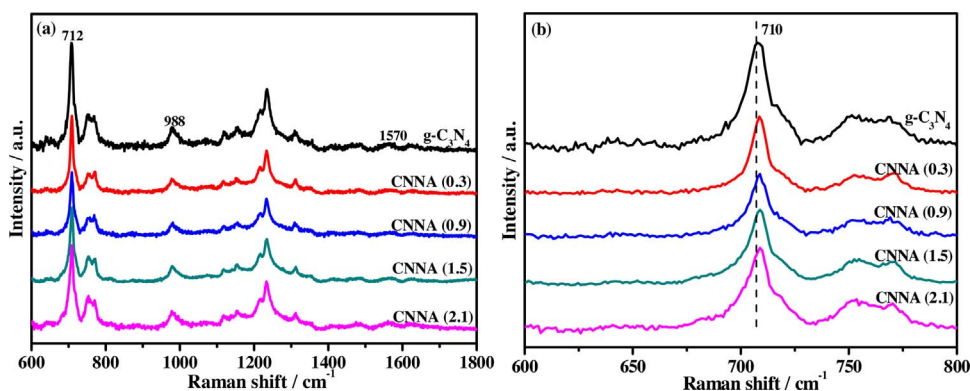


Fig. 4. Raman spectra (a) and partial magnification of the characteristic peaks (b) of pure  $g\text{-C}_3\text{N}_4$  and CNNA system.

peak centered at 397.9 eV could be assigned to the presence of pyridinic-N species, referring to the  $sp^2$  nitrogen atoms ( $N_{2c}$ ) of triazine rings in  $\text{C}=\text{N}=\text{C}$ . The peak at 398.7 eV corresponded to three-coordinated nitrogen atoms ( $N_{3c}$ ), trigonally bonded with  $sp^3\text{C}$  atoms. Besides, the peak located at 400.4 eV was ascribed to the terminal amino groups ( $-\text{NH}_x$ ) of  $g\text{-C}_3\text{N}_4$ . Interestingly, the peak area ratio of the  $N_{\text{NH}_x}$  to the  $N_{3c}$  ( $N_{\text{NH}_x}/N_{3c}$ ) decreased from 0.60 to 0.51 for  $g\text{-C}_3\text{N}_4$  and CNNA (0.9) (Table 1), indicating the loss of N atoms occurs at the uncondensed terminal  $\text{NH}_x$  species after calcinating nitric acid treatment of melamine as a precursor and nitrogen vacancies could generated on  $g\text{-C}_3\text{N}_4$  due to the deficiency of  $\text{NH}_x$  species, which was similar to the result of literature reported previously [37]. Additionally, as shown in Fig. S3, the valence band energy of CNNA(0.9) was 1.57 eV, which was the same as that of pure  $g\text{-C}_3\text{N}_4$ . The corresponding conduction bands of  $g\text{-C}_3\text{N}_4$  and CNNA (0.9) were calculated to be  $-1.13$  eV and  $-0.88$  eV, respectively. The phenomenon illustrated that nitrogen vacancies in the  $g\text{-C}_3\text{N}_4$  potentially resulted in a partial overlap of additional electron states in the conduction band, attributed to the formation of mid-gap states that validates the slightly narrowed bandgap by nitrogen vacancies. To further certify the deficiency of N-containing species on the framework of  $g\text{-C}_3\text{N}_4$ , elemental analysis was carried out. As shown in Table S2, the N/C atomic ratio of CNNA samples was lower than that of pristine  $g\text{-C}_3\text{N}_4$ . This result directly suggested that the existence of nitrogen vacancies in the framework of  $g\text{-C}_3\text{N}_4$ . Meanwhile, H/C atomic ratio of CNNA samples and  $g\text{-C}_3\text{N}_4$  further illustrated that nitrogen vacancies mainly arised from the deficiency of  $\text{NH}_x$  species, matched well with the results of XPS.

### 3.2. Photocatalytic performance of CNNA (X) samples

For the first time, the CNNA (X) samples were used as photocatalysts for the selective aerobic oxidation of benzyl alcohol to benzaldehyde by using molecular oxygen as the oxidant and acetonitrile as the solvent under simulated sunlight irradiation. As shown in Table 2, the

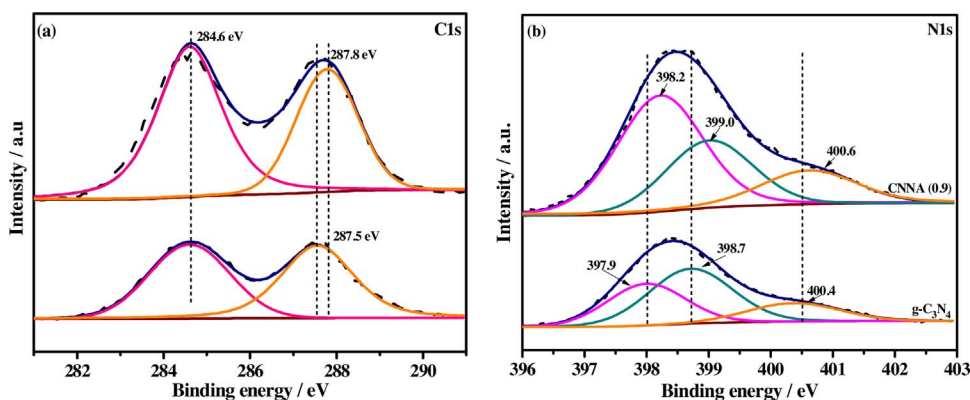


Fig. 5. XPS spectra of pure  $g\text{-C}_3\text{N}_4$  and CNNA systems: (a) high-resolution C1s; (b) high-resolution N1s.

Table 1

The deconvolution result of N1s XPS spectra of  $g\text{-C}_3\text{N}_4$  and CNNA (0.9).

	$g\text{-C}_3\text{N}_4$			CNNA (0.9)		
	$N_{2c}$	$N_{3c}$	$N_{\text{NH}_x}$	$N_{2c}$	$N_{3c}$	$N_{\text{NH}_x}$
Peak/eV	397.9	398.7	400.4	398.2	399.0	400.6
FWHM	1.576	1.472	1.740	1.620	1.635	1.739
Area	3216	2200	1118	7151	4001	1945
Molar ratio ( $N_{\text{NH}_x}/N_{3c}$ )	0.60			0.51		

controlled experiments exhibited that merely a negligible reaction occurred in dark or without the photocatalyst (entries 1 and 2). However, the photocatalytic oxidation performance of the light-excited CNNA (X) samples had obviously enhanced. In comparison with pure  $g\text{-C}_3\text{N}_4$ , a significant improvement in the photooxidation activity was obtained by the nitrogen vacancies in the framework structure of  $g\text{-C}_3\text{N}_4$  sample. Moreover, benzaldehyde yield was strongly dependent on the amount of nitrogen vacancies in the CNNA system. Obviously, CNNA (0.9) was the optimum photocatalyst for this reaction with 68.3% benzyl alcohol conversion and almost 100% selectivity (entry 5). When CNNA samples achieved by the mole ratio of nitric acid to melamine higher than 0.9, obvious decrease of  $S_{\text{BET}}$  and  $N_{\text{NH}_x}$  vacancies occurred, together with the drop of benzyl alcohol conversion (from 68.3% to 51.6%) (entries 6 and 7).

The effect of reaction conditions (such as reaction temperature, solvent, reaction time) on photocatalytic activity were investigated in depth. When the reaction temperature was increased from 298 K to 328 K (entries 5 and 11–13), the conversion of benzyl alcohol increased first and then decreased. This phenomenon may be attributed to the slower of thermal motion of substrate molecule under lower temperature ( $< 308$  K) and the thermal decomposition of actual oxidant ( $\text{H}_2\text{O}_2$ ) under higher temperature ( $> 308$  K) [38]. Therefore, 308 K was selected as the optimal reaction temperature for further studied. Moreover, with other conditions fixed, the photocatalytic performance of

**Table 2**  
Photooxidation of benzyl alcohol by various catalysts under different conditions.<sup>a</sup>

Entry	Catalyst	S <sub>BET</sub> (m <sup>2</sup> /g)	Solvent	Temperature (K)	Sunlight	Conv. (%)	Sel. (%)
1	no catalyst	—	acetonitrile	308	+	0.3	trace
2	CNNA (0.9)	23.4	acetonitrile	308	—	1.3	> 99
3	g-C <sub>3</sub> N <sub>4</sub>	12.2	acetonitrile	308	+	36.3	> 99
4	CNNA (0.3)	21.6	acetonitrile	308	+	55.5	> 99
5	CNNA (0.9)	23.4	acetonitrile	308	+	68.3	> 99
6	CNNA (1.5)	18.0	acetonitrile	308	+	53.5	> 99
7	CNNA (2.1)	17.5	acetonitrile	308	+	51.6	> 99
8	CNNA (0.9)	23.4	dimethyl carbonate	308	+	61.8	> 99
9	CNNA (0.9)	23.4	tributyl phosphate	308	+	92.8	16.4
10	CNNA (0.9)	23.4	trifluorotoluene	308	+	55.6	> 99
11	CNNA (0.9)	23.4	acetonitrile	298	+	61.4	> 99
12	CNNA (0.9)	23.4	acetonitrile	318	+	57.4	> 99
13	CNNA (0.9)	23.4	acetonitrile	328	+	51.3	> 99

<sup>a</sup> Reaction condition: catalyst, 20 mg; benzyl alcohol, 1 mmol; solvent, 10 mL; oxidizing agent: molecular oxygen; reaction time, 9 h; desired product: benzaldehyde.

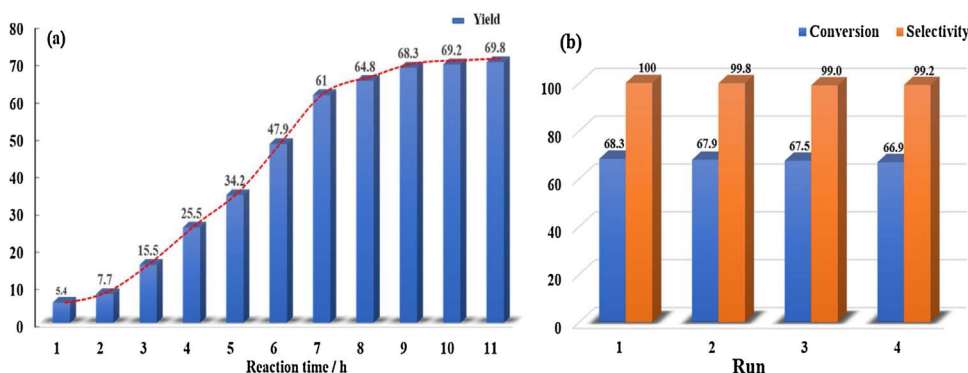


**Fig. 6.** The influence of reaction time on the selective oxidation of benzyl alcohol over CNNA (0.9) (a) and the cycling runs at the photooxidation of benzyl alcohol over CNNA (0.9) (b).

CNNA (0.9) in various representative solvents were explored (Table 2, entries 5 and 8–10). The comparisons revealed that acetonitrile was the best solvent for the photooxidation reaction with the benzyl alcohol conversion up to 68.3% and benzaldehyde selectivity over 99%. To our knowledge, acetonitrile as solvent not only possessed the strong polarity, but also owned good dissolvent ability of oxygen [39,40]. In addition, Fig. 6a and Table S3 showed the photocatalytic selective oxidation of benzyl alcohol on CNNA (0.9) catalyst as a function of reaction time. When increasing reaction time, the conversion gradually increased. It was a remarkable observation that the highest conversion of 68.3% and selectivity over 99% could be obtained when the reaction time was 9 h. With further prolonging the reaction time, no obvious change was observed.

The substrate scope of the aerobic oxidation of aromatic alcohols over CNNA sample was extended under similar reaction conditions, and the corresponding results were summarized in Table 3. Remarkably, benzyl alcohols with electron-donating groups (–CH<sub>3</sub> and –OCH<sub>3</sub>)

**Table 3**  
Photooxidation of aromatic alcohols to corresponding aromatic aldehydes over CNNA (0.9) photocatalyst.<sup>a</sup>

Entry	–R	Conv. (%)	Sel. (%)
1	–CH <sub>3</sub>	79.1	> 99
2	–OCH <sub>3</sub>	85.7	> 99
3	–H	68.3	> 99
4	–NO <sub>2</sub>	57.5	> 99
5	–Cl	61.4	> 99

<sup>a</sup> Reaction condition: catalyst, 20 mg; aromatic alcohol, 1 mmol; solvent: acetonitrile, 10 mL; oxidizing agent: molecular oxygen; reaction time, 9 h; reaction temperature, 308 K.

substituted on the opposite of –CH<sub>2</sub>OH group of the phenyl ring positively affected the conversion. Whereas, those with electron-withdrawing groups exhibited slightly reduced conversion. The above phenomenon matched well with the literature reported previously [41,42] and further confirmed that electron-donating groups contributed to the production of electron-deficient intermediates in the redox process, accelerating the photocatalytic oxidation of aromatic alcohols to the corresponding aldehydes.

To further investigate the photocatalytic performance of CNNA system, the photodegradation of organic pollutants (RhB and MO) was chosen. As shown in Fig. S4, CNNA (0.9) sample exhibited higher photocatalytic activity than that of other CNNA system and pristine g-C<sub>3</sub>N<sub>4</sub>. Hence, it could be implied that CNNA (0.9) was also an excellent candidate for the photocatalytic degradation of common pollutants.

### 3.3. Stability evaluation of CNNA photocatalyst

To illustrate the reusability of the CNNA (0.9) photocatalyst in the selective aerobic oxidation of aromatic alcohols to the corresponding aldehydes, a four-cycle experiment was carried out. Each repeated reaction cycle under the same condition was described as follows. After each cycle, the catalyst was recovered by simple filtration, washed with water and ethanol three times, then dried at 100 °C for 12 h and reused in the next run. As shown in Fig. 6b, the conversion of benzyl alcohol and the selectivity of benzaldehyde almost kept constant in the three runs in succession. Meanwhile, there was no distinction between the XRD results before and after reaction (see Fig. S5), suggesting its structural stability during the photocatalytic oxidation process.

### 3.4. Possible photooxidation mechanism

The separation efficiency of photogenerated electron-hole pairs of g-C<sub>3</sub>N<sub>4</sub> based photocatalysts was investigated by photoluminescence (PL)

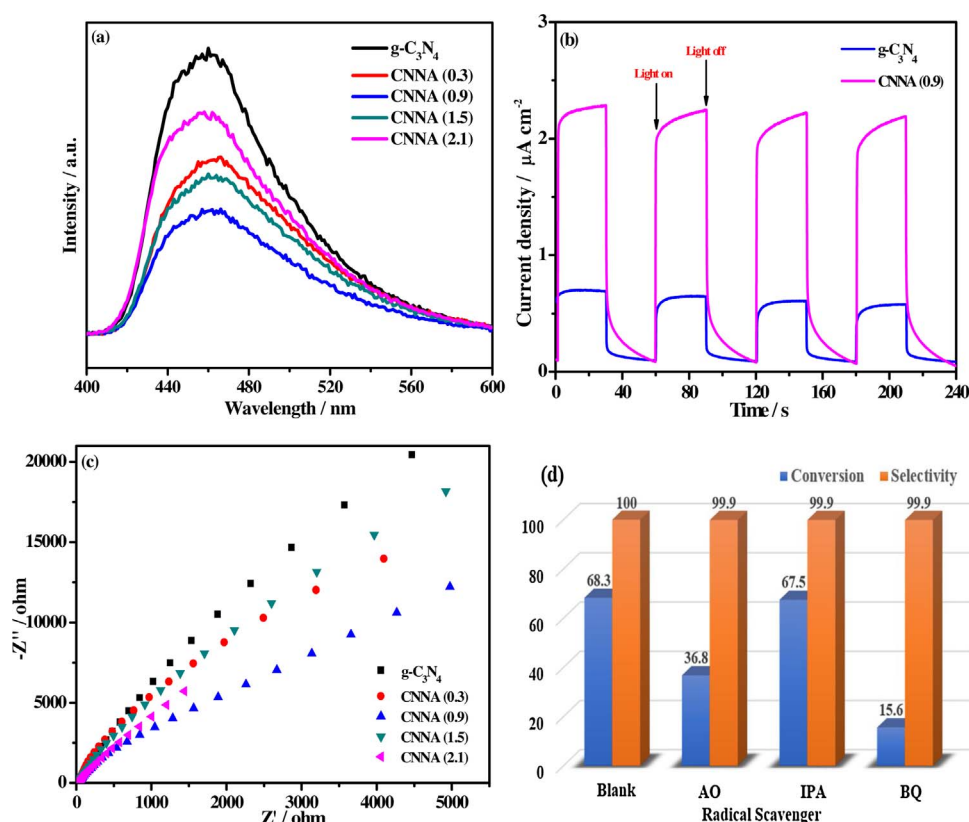


Fig. 7. Photoluminescence emission spectra (a), Transient photocurrent (b) and Nyquist plots of the impedance spectra (c) of pure g-C<sub>3</sub>N<sub>4</sub> and CNNA systems and the effects of different reactive species scavengers on the photocatalytic oxidation of benzyl alcohol over CNNA (0.9) photocatalyst.

spectra. Fig. 7a exhibited the PL spectra of pure g-C<sub>3</sub>N<sub>4</sub> and CNNA (X) samples under the excitation wavelength of 365 nm. Obviously, the samples displayed a main peak centered at approximately 460 nm, ascribed to the direct electrons and holes recombination of band transition. Compared to pristine g-C<sub>3</sub>N<sub>4</sub>, the PL intensities of CNNA samples decreased, suggesting that the introduction of nitrogen vacancies contribute to retarding the recombination of photogenerated electron-hole pairs due to the nitrogen vacancies as electron or hole traps. Moreover, CNNA (0.9) catalyst exhibited the lowest PL emission peak, indicating that CNNA (0.9) sample displayed the lowest recombination probability of photogenerated charge carriers, which was well consistent with the results of photocatalytic oxidation performance. The transient photocurrent responses via four on-off cycles of g-C<sub>3</sub>N<sub>4</sub> and CNNA (X) electrodes were tested to further study the recombination probability of photogenerated charge carriers (Fig. 7b). The photocurrent of CNNA (0.9) was higher than that of pure g-C<sub>3</sub>N<sub>4</sub>, ulteriorly illustrating that the introduction of nitrogen vacancies into the framework of g-C<sub>3</sub>N<sub>4</sub> helped improve the separation efficiency of photogenerated electrons and holes, thus enhancing the photocatalytic activity. The time-resolved transient PL spectra were so important for the illustration of the dynamic behavior of photogenerated electrons for both pristine g-C<sub>3</sub>N<sub>4</sub> and CNNA (0.9) samples [17,43,44]. As shown in Fig. S6, the PL decay lifetime of pure g-C<sub>3</sub>N<sub>4</sub> was shorter than that of CNNA (0.9) and the corresponding intensity-average lifetimes ( $\tau$ ) of g-C<sub>3</sub>N<sub>4</sub> and CNNA (0.9) samples were calculated to be 4.41 ns and 4.61 ns, respectively. Hence, the above time-resolved fluorescence results further illustrated that the introduction of nitrogen vacancies in the g-C<sub>3</sub>N<sub>4</sub> matrix could efficiently enhance electron transport and retard the recombination of photogenerated electron and hole pairs.

To further understand the role of nitrogen vacancies in the CNNA (X) systems, electrochemical impedance spectroscopy (EIS) Nyquist plots were carried out in a frequency range from 10<sup>-1</sup> Hz to 10<sup>6</sup> Hz, as shown in Fig. 7c. Compared with pure g-C<sub>3</sub>N<sub>4</sub>, the Nyquist plots of the CNNA samples displayed smaller diameter of the inconspicuous arcs in the high-frequency region, indicating the lower electronic resistance of

the CNNA photocatalysts. Meanwhile, it could be clearly seen that CNNA (0.9) sample exhibited the smallest diameter in all the samples. Therefore, the nitrogen vacancies introduced significantly enhanced the electron mobility and electrons and holes separation of g-C<sub>3</sub>N<sub>4</sub>.

In order to further get insights into the reaction mechanism for photocatalytic selective oxidation of benzyl alcohol over CNNA (0.9) photocatalyst, a series of controlled experiments with different radical scavengers were carried out and the corresponding results are shown in Fig. 7d. In this study, ammonium oxalate (AO), isopropanol (IPA) and 1,4-benzoquinone (BQ) are used as the scavengers for holes (h<sup>+</sup>), hydroxyl radicals ( $\cdot$ OH) and superoxide radical ( $\cdot$ O<sub>2</sub><sup>-</sup>), respectively [45]. When BQ was introduced in the reaction system, the conversion of benzyl alcohol was remarkably suppressed (68.3%–15.6%), indicating that  $\cdot$ O<sub>2</sub><sup>-</sup> should be the main active species for the photooxidation of benzyl alcohol. Simultaneously, when AO was added into the reaction system, a certain decrease of the conversion of benzyl alcohol appeared (68.3%–36.8%), suggesting that h<sup>+</sup> also plays a key role in the photocatalytic oxidation process. Whereas the photocatalytic oxidation performance of CNNA (0.9) sample kept almost no change by the addition of IPA (68.3%–67.5%). Therefore, it could be concluded that the photocatalytic selective oxidation of benzyl alcohol to benzaldehyde by CNNA photocatalyst was primarily triggered by the superoxide radicals and the holes.

On the basis of the above results, a possible mechanistic proposal for the photooxidation process of aromatic alcohols over CNNA system was given in Fig. 8. Under simulated sunlight irradiation, CNNA sample was excited to generate electrons and holes. The holes (h<sup>+</sup>) on the valence band activated the absorbed aromatic alcohols to generate aromatic alcohols cation radicals. Meanwhile, the photogenerated electrons from conduction band of g-C<sub>3</sub>N<sub>4</sub> was strong enough to reduce molecular oxygen to  $\cdot$ O<sub>2</sub><sup>-</sup> and then produced superoxide ( $\cdot$ OOH) radicals. Moreover, the nitrogen-neighboring carbon in g-C<sub>3</sub>N<sub>4</sub> owned a metal-like d band electronic structure and made the adjacent carbon more capable to host the formation of reaction oxygen species and be a stable adsorption site of peroxide-like species [46]. Subsequently, the

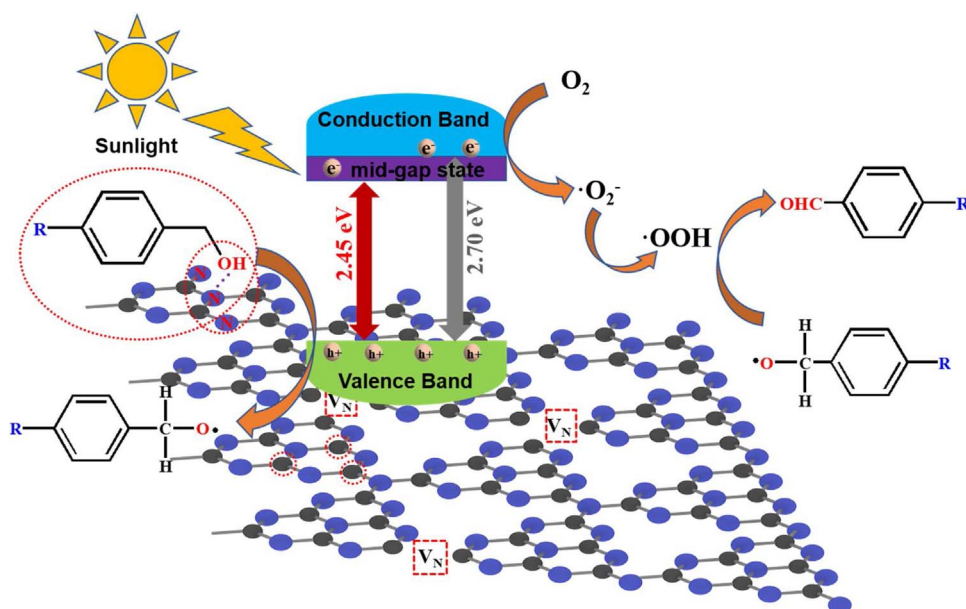


Fig. 8. The possible mechanism for photocatalytic selective oxidation of aromatic alcohols to corresponding aldehydes over CNNA system.

obtained superoxide radicals interacted with aromatic alcohols cation radicals to create corresponding aromatic aldehydes. Notably, defective g-C<sub>3</sub>N<sub>4</sub> could provide a number of nitrogen-containing groups on their surface and made aromatic alcohols easy access to its active sites through hydrogen bonding [19]. The introduction of nitrogen vacancy sites resulted in a partial overlap of defect-related states, conducive to the narrowing of the band gap of g-C<sub>3</sub>N<sub>4</sub> and the enhancement of optical absorption. Meanwhile, the nitrogen vacancies in the framework of g-C<sub>3</sub>N<sub>4</sub> could act as electron or hole traps, facilitating the separation efficiency of photogenerated electrons and holes. The higher surface area was also favor of more reactive active sites, which was beneficial to the photocatalytic oxidation of aromatic alcohols [47,48].

#### 4. Conclusion

In summary, defective g-C<sub>3</sub>N<sub>4</sub> nanosheets were successfully synthesized by high-temperature thermal condensation of nitric acid-pre-treated melamine as a precursor. The obtained CNNA sample showed excellent photocatalytic oxidation performance for the aerobic oxidation of aromatic alcohols with molecular oxygen under simulated sunlight, far exceeding that of pristine g-C<sub>3</sub>N<sub>4</sub>. The introduction of nitrogen vacancies at the uncondensed terminal NH<sub>x</sub> lattice sites in the framework of g-C<sub>3</sub>N<sub>4</sub> contributed to the enhancement of optical absorption and the increase of surface area and simultaneously acted as electron or hole traps that enhanced the separation efficiency of photogenerated electron-hole pairs, thus obviously improving the photocatalytic oxidation activity. The present study put forward a promising strategy to design defective g-C<sub>3</sub>N<sub>4</sub> and highlighted the important role of nitrogen vacancy on the electronic structure and chemical properties of g-C<sub>3</sub>N<sub>4</sub> and its photooxidation activity, which might open novel vistas for exploring defective semiconductors in various solar energy applications, such as pollutant degradation, CO<sub>2</sub> photofixation and photosynthesis.

#### Acknowledgments

We would like to thank financial support by the National Natural Science Foundation of China (No. 21476110, No. 21706131), the Natural Science Foundation of Jiangsu Province of China (No. BK20151531), the Key Project for University Natural Science Foundation of Jiangsu Province (No. 14KJA530001) and Natural Science Fund for Colleges and Universities in Jiangsu Province (No. 17KJB530004).

#### Appendix A. Supplementary data

Supplementary data associated with this article can be found, in the online version, at <http://dx.doi.org/10.1016/j.apcatb.2017.09.048>.

#### References

- [1] H. Li, F. Qin, Z.P. Yang, X.M. Cui, J.F. Wang, L.Z. Zhang, J. Am. Chem. Soc. 139 (2017) 3513–3521.
- [2] C.X. Zheng, G.P. He, X. Xiao, M.L. Lu, H. Zhong, X.X. Zuo, J.M. Nan, Appl. Catal. B: Environ. 205 (2017) 201–210.
- [3] E. Gaster, S. Kozuch, D. Pappo, Angew. Chem. Int. Ed. 56 (2017) 5912–5915.
- [4] M.E. González-Núñez, R. Mello, A. Olmos, R. Acerete, G. Asensio, J. Org. Chem. 71 (2006) 1039–1042.
- [5] R. Liu, X. Liang, C. Dong, X. Hu, J. Am. Chem. Soc. 126 (2004) 4112–4113.
- [6] J. Lou, M. Wang, L.-Y. Zhu, Z. Fang, Catal. Commun. 4 (2003) 647–649.
- [7] G.C. Behera, K.M. Parida, Appl. Catal. A: Gen. 413–414 (2012) 245–253.
- [8] M.T. Qamar, M. Aslam, Z.A. Rehan, M.T. Soomro, J.M. Basahi, I.M.I. Ismail, T. Almeelbi, T. Almeelbi, A. Hameed, Appl. Catal. B: Environ. 201 (2017) 105–118.
- [9] J. Ding, L. Zhang, Q.Q. Liu, W.L. Dai, G.F. Guan, Appl. Catal. B: Environ. 203 (2017) 335–342.
- [10] C. Gao, J. Wang, H.X. Xu, Y.J. Xiong, Chem. Soc. Rev. 46 (2017) 2799–2823.
- [11] L. Mohapatra, K. Parida, J. Mater. Chem. A 4 (2016) 10744–10766.
- [12] W.X. Zou, L. Zhang, L.C. Liu, X.B. Wang, J.F. Sun, S.G. Wu, Y. Deng, C.J. Tang, F. Gao, L. Dong, Appl. Catal. B: Environ. 181 (2016) 495–503.
- [13] W.J. Ong, L.L. Tan, S.P. Chai, S.T. Yong, A.R.A. Mohamed, Nanoscale 6 (2014) 1946–2008.
- [14] M. Zeng, Y.Z. Li, M.Y. Mao, J.L. Bai, L. Ren, X.J. Zhao, ACS Catal. 5 (2015) 3278–3286.
- [15] M.V. Sheridan, D.J. Hill, B.D. Sherman, D. Wang, S. Marquard, K.R. Wee, J.F. Cahoon, T.J. Meyer, Nano Lett. 17 (2017) 2440–2446.
- [16] L.C. Liu, C.Y. Ge, W.X. Zou, X.R. Gu, F. Gao, L. Dong, Phys. Chem. Chem. Phys. 17 (2015) 5133–5140.
- [17] L.C. Liu, Z.Y. Ji, W.X. Zou, X.R. Gu, Y. Deng, F. Gao, C.J. Tang, L. Dong, ACS Catal. 3 (2013) 2052–2061.
- [18] L.C. Liu, X.R. Gu, Z.Y. Ji, W.X. Zou, C.J. Tang, F. Gao, L. Dong, J. Phys. Chem. C 117 (2013) 18578–18587.
- [19] J. Ding, Q.Q. Liu, Z.Y. Zhang, X. Liu, J.Q. Zhao, S.B. Cheng, B.N. Zong, W.L. Dai, Appl. Catal. B: Environ. 165 (2015) 511–518.
- [20] X.Y. Pan, X.X. Chen, Z.G. Yi, ACS Appl. Mater. Interfaces 8 (2016) 10104–10108.
- [21] F.F. Liang, Y.F. Zhu, Appl. Catal. B: Environ. 180 (2016) 324–329.
- [22] W.X. Zou, Y. Shao, Y. Pu, Y.D. Luo, J.F. Sun, K.L. Ma, C.J. Tang, F. Gao, L. Dong, Appl. Catal. B: Environ. 218 (2017) 51–59.
- [23] S.W. Cao, Q. Huang, B.C. Zhu, J.G. Yu, J. Power. Sources 351 (2017) 151–159.
- [24] B. Liu, L.C. Bai, E.A. Korznikova, S.V. Dmitriev, A.W.K. Law, K. Zhou, J. Phys. Chem. C 121 (2017) 13876–13887.
- [25] Y. Yamada, K. Murta, R. Fujita, J.P. Kim, A. Watanabe, M. Nakamura, S. Sato, K.J. Hata, P. Ercius, J. Ciston, C.Y. Song, K. Kim, W. Regan, W. Ganett, A. Zettl, J. Am. Chem. Soc. 136 (2014) 2232–2235.
- [26] S.S. Wang, Z. Qin, G.S. Jung, F.J.M. Matinez, K. Zhang, M.J. Buehler, J.H. Warner, ACS Nano 10 (2016) 9831–9839.
- [27] L.L. Li, X.F. Yu, X.J. Yang, Y. Fang, X.H. Zhang, X.W. Xu, P. Jin, C.C. Tang, J. Mater. Chem. A 4 (2016) 15631–15637.



- [28] Q.L. Tang, P. Kanhere, C.F. Ng, S. Chen, S. Chakraborty, A.C.H. Huan, T.C. Sum, R. Ahuja, Z. Chen, *Chem. Mater.* 27 (2015) 4930–4933.
- [29] Z.H. Hong, B. Shen, Y.L. Chen, B.Z. Lin, B.F. Gao, *J. Mater. Chem. A* 1 (2013) 11754–11761.
- [30] P.J. Yang, H.H. Ou, Y.X. Fang, X.C. Wang, *Angew. Chem. Int. Ed.* 56 (2017) 3992–3996.
- [31] D.D. Zheng, X.N. Cao, X.C. Wang, *Angew. Chem. Int. Ed.* 55 (2016) 11512–11516.
- [32] P. Liu, G. Liu, H.M. Cheng, *J. Phys. Chem. C* 116 (2012) 11013–11018.
- [33] Q. Liu, T.X. Chen, Y.R. Guo, Z.G. Zhang, X.M. Fang, *Appl. Catal. B: Environ.* 193 (2016) 248–258.
- [34] J. Ding, L. Wang, Q.Q. Liu, Y.Y. Chai, X. Liu, W.L. Dai, *Appl. Catal. B: Environ.* 176–177 (2015) 91–98.
- [35] P. Wu, J.R. Wang, J. Zhao, L.J. Guo, F.E. Osterloh, *J. Mater. Chem. A* 2 (2014) 20338–20344.
- [36] N. Tian, Y.H. Zhang, X.W. Li, K. Xiao, X. Du, F. Dong, G.I.N. Waterhouse, T. Zhang, H.W. Huang, *Nano Energy* 38 (2017) 72–81.
- [37] J.S. Kim, J.W. Oh, S.I. Woo, *Catal. Commun.* 293–294 (2017) 8–14.
- [38] Y. Shiraishi, S. Kanazawa, Y. Sugano, D. Tsukamoto, H. Sakamoto, S. Ichikawa, T. Hirai, *ACS Catal.* 4 (2014) 774–780.
- [39] L.H. Yu, Y.M. Lin, D.Z. Li, *Appl. Catal. B: Environ.* 216 (2017) 88–94.
- [40] Q. Wu, Y.M. He, H.L. Zhang, Z.Y. Feng, Y. Wu, T.H. Wu, *Mol. Catal.* 436 (2017) 10–18.
- [41] B.H. Long, Z.X. Ding, X.C. Wang, *ChemSusChem* 6 (2013) 2074–2078.
- [42] Y.H. Fu, L. Sun, H. Yuan, L. Xu, F.M. Zhang, W.D. Zhu, *Appl. Catal. B: Environ.* 187 (2016) 212–217.
- [43] G.G. Zhang, A. Savateev, Y.B. Zhao, L. Li, M. Antonietti, *J. Mater. Chem. A* 5 (2017) 12723–12728.
- [44] Q. Liu, T.X. Chen, Y.R. Guo, Z.G. Zhang, X.M. Fang, *Appl. Catal. B: Environ.* 193 (2016) 248–258.
- [45] L. Zhou, L.Z. Wang, J.Y. Lei, Y.D. Liu, J.L. Zhang, *Catal. Commun.* 89 (2017) 125–128.
- [46] W.J. Li, Y.J. Gao, W.L. Chen, P. Tang, W.Z. Li, Z.J. Shi, D.S. Su, J.G. Wang, D. Ma, *ACS Catal.* 4 (2014) 1261–1266.
- [47] F.Z. Su, S.C. Mathew, G. Lipner, X.Z. Fu, M. Antonietti, S. Blechert, X.C. Wang, *J. Am. Chem. Soc.* 132 (2010) 16299–16301.
- [48] Y. Shiraishi, S. Kanazawa, Y. Sugano, D. Tsukamoto, H. Sakamoto, S. Ichikawa, T. Hirai, *ACS Catal.* 4 (2014) 774–780.